Journal of Materials Chemistry A

ROYAL SOCIETY OF CHEMISTRY

PAPER

View Article Online
View Journal | View Issue

Cite this: *J. Mater. Chem. A*, 2022, **10**, 14540

Operando synchrotron X-ray studies of MnVOH@SWCNT nanocomposites as cathodes for high-performance aqueous zinc-ion batteries†

Sanna Gull, Shao-Chu Huang, Chung-Sheng Ni, Shih-Fu Liu, Wei-Hsiang Lin and Han-Yi Chen *

Aqueous zinc-ion batteries (AZIBs) have great potential as energy-storage devices because of their low cost and environmental friendliness. However, the key challenge for rapid and reversible Zn^{2+} for AZIBs is the generation of a stable and efficient cathode material. Herein, we prepared a scalable synthesis method, based on a low-temperature (120 °C) hydrothermal route, to prepare $Mn_{0.19}V_2O_5{\cdot}2.34H_2O$ (MnVOH), which was incorporated into a single-walled carbon nanotube (SWCNT) network, and subsequently utilized as the AZIB cathode material. Furthermore, the MnVOH@SWCNT nanocomposite material ensured close interaction between MnVOH and SWCNTs, with a continuous network structure, and expanded interlayer spacing that provided fast electron transfer kinetics ($D_{Zn}{}^{2+}$: 10^{-11} to 10^{-12} cm^2 s^{-1}). This resulted in an excellent rate performance of 81% during cycling. Consequently, the resultant batteries possessed a significantly enhanced intercalation storage capacity of 381 mA h g^{-1}, at a current density of 0.1 A g^{-1}, and reduced polarization with a high capacity retention of 89% over 300 cycles (at 5 A g^{-1}). Furthermore, *operando* synchrotron X-ray absorption near-edge spectroscopy (XANES) was studied for the first time to verify the Zn^{2+} charge-storage mechanism. To further understand the structural changes of the MnVOH@SWCNT nanocomposite during the discharge/charge process, *operando* synchrotron X-ray diffraction (XRD) measurements were also performed. In addition, the MnVOH@SWCNT nanocomposite material could sustain a high energy density of *ca.* 194 W h kg^{-1} at a high-power density of 3.2 kW kg^{-1}, which is higher than that of MnVOH, thus demonstrating that MnVOH@SWCNTs is a promising candidate as a high-performance cathode material for AZIB applications.

Received 5th April 2022
Accepted 7th June 2022

DOI: 10.1039/d2ta02734h

rsc.li/materials-a

Introduction

Increasing energy demands and environmental sustainability concerns have raised the standards for next-generation energy storage technologies.[1–4] Lithium-ion batteries (LIBs) with organic electrolytes have attained economic success owing to their light weight and high energy density properties.[5] However, these batteries are still too expensive for grid-scale energy storage. The use of volatile organic electrolytes in large energy storage systems is a serious ecological safety concern. Hence, the economics, resource limitations, and safety concerns of such battery systems have prompted research on other reliable and efficient alternatives.[6] Rechargeable aqueous batteries offer the advantage of low production costs, and the electrolyte used is highly safe. These reversible aqueous batteries, primarily aqueous zinc-ion batteries (ZIBs), are new energy storage possibilities that have garnered considerable attention in recent years because of the following attributes: (i) the mechanism of two-electron transfer during intercalation/deintercalation that produces high energy density; (ii) non-flammable electrolyte ensuring operational safety; and (iii) high ionic conductivity of aqueous electrolytes (~1 S cm^{-1}), which is more than two orders of magnitude higher than that of organic electrolytes (1–10 mS cm^{-1}). Further, the zinc metal which can directly be used as an anode material can be found in significant amounts (79 ppm) in the Earth's crust, has a high theoretical capacity (820 mA h g^{-1}), and low redox potential of Zn/Zn^{2+} (−0.76 V *vs.* the standard hydrogen electrode).[7,8] Moreover, the development of suitable cathode materials for rechargeable AZIBs is a global priority. Advanced material characterization techniques, such as *in situ*/*operando* measurements, can help in material selection and in-depth material analysis during the electrochemical reactions occurring in ZIBs.

In the last few years, numerous cathode materials have been developed for zinc-ion battery systems, including manganese compounds, Prussian blue analogs, organic compounds, and vanadium oxides, as shown in Table S1.† Manganese oxides, with a comparatively higher working voltage of 1.3–1.4 V, deliver a capacity of 285 mA h g^{-1}. However, the formation of

Department of Materials Science and Engineering, National Tsing Hua University, 101, Sec. 2, Kuang-Fu Road, Hsinchu 30013, Taiwan. E-mail: hanyi.chen@mx.nthu.edu.tw

† Electronic supplementary information (ESI) available. See https://doi.org/10.1039/d2ta02734h

irreversible phase change and dissolution of Mn^{3+} during cycling is still a serious concern.[9] Prussian blue analog materials exhibit an open framework structure and mixed-valence hexacyanoferrate tunable structure that allows rapid ion diffusion. However, the less tunable chemical state of the redox ions limits the capacity to less than 100 mA h g^{-1}.[10] In addition, organic material-based compounds exhibit a working voltage of 1.0–1.1 V and a soft lattice; however, the solubility of electrolytes is still a major challenge.[11] Vanadium-based compounds,[12–17] especially layered vanadates, have attracted more attention owing to their wide range of valence states (from V^{3+} to V^{5+}), which are favorable for multielectron transfer. The resultant AZIBs show a superior capacity of ~380 mA h g^{-1} and can simultaneously provide low prices owing to the abundance of vanadium on Earth. The standard reaction mechanism in vanadium-based ZIBs is insertion/extraction where Zn^{2+} is inserted in the host material during cycling.[18] However, the energy storage mechanisms for aqueous zinc-ion battery systems are more controversial and challenging than the Zn^{2+} insertion reaction mechanism, such as Zn^{2+}/H^{+} (individual insertion or co-insertion of Zn^{2+} and H^{+}), chemical conversion reactions, and dissolution–deposition reactions.[19,20] Recently, with molecules/ions such as Al^{3+},[12] Mg^{2+},[13] Zn^{2+},[14] Ca^{2+},[15] Cu^{2+},[21] Mn^{2+},[22] Li^{+},[23] Na^{+},[24] K^{+},[7] H_2O,[25] and polyaniline introduced into the vanadium layers,[26] the formed layered vanadium-based compounds have attracted great attention because of the tunable interlayer spacing along with the presence of crystal water that helps to stabilize the crystal structure during the Zn^{2+} transport process during cycling. A series of hydrated vanadates have been studied as cathode materials for ZIBs, including $Al_{0.84}V_{12}O_{30.3}\cdot nH_2O$,[12] $Mg_{0.34}V_2O_5\cdot nH_2O$,[13] $Zn_{0.25}V_2O_5\cdot nH_2O$,[14] $CaV_6O_{16}\cdot 3H_2O$,[15] $Li_xV_2O_5\cdot nH_2O$,[23] and $KV_{12}O_{30-y}\cdot nH_2O$[7] and they have become the most competitive cathode materials for ZIBs. Moreover, among the various metal-ion-intercalated vanadium oxides, Mn-doped V_2O_5 has recently been utilized several times and is considered a promising cathode material for AZIBs. The first report from Liu *et al.* revealed that the chemically inserted Mn^{2+} cations could act as structural pillars, and the expanded interplanar spacing of 12.9 Å can collectively promote fast zinc ion intercalation. Thus, the AZIBs delivered a specific capacity of 260 mA h g^{-1} at 4 A g^{-1}.[22] Another research study by Kurungot *et al.* reported a surface-assisted route for preparing Mn-doped hydrated V_2O_5 which delivered a capacity of 341 mA h g^{-1} at 0.1 A g^{-1}.[27] Very recently, Li's group used density functional theory (DFT) calculations and demonstrated that $Mn_{0.15}V_2O_5\cdot nH_2O$ composites, with a narrow direct energy bandgap, significantly improved the electrochemical performance and exhibited a high specific capacity of 367 mA h g^{-1} at 0.1 A g^{-1} in zinc-ion battery cathodes.[28] These studies demonstrated that Mn-doped V_2O_5 materials have outstanding electrochemical properties, indicating that introducing Mn into the layers of V-based oxides can significantly stabilize the crystal structures and improve the electrochemical properties of AZIB cathodes. Nevertheless, to the best of our knowledge, the charge-storage mechanism of these materials has not yet been explored in detail.

Furthermore, the electronic conductivities of hydrated vanadates are generally low, and the sluggish Zn ion diffusion kinetics during the electrochemical reaction results in slow reaction kinetics.[29,30] To enhance the conductivity of such active materials, various studies have been undertaken on vanadium-based ZIBs, and the introduction of highly conductive materials has achieved remarkable achievements.[16,17,31–38] For example, Wan *et al.* designed $KV_3O_8\cdot 0.75H_2O$/SWCNT (KVO/SWCNT) composite films and used them as cathodes for ZIBs. Compared with pristine KVO, the KVO/SWCNT composite exhibits better rate retention and cycling performance, with a higher discharge specific capacity of 379 mA h g^{-1} at 0.1 A g^{-1}.[36] Recently, Sun *et al.* used a simple one-pot hydrothermal process to synthesize Mn^{2+} inserted hydrated vanadium pentoxide nanobelts/reduced graphene oxide ($Mn_xV_2O_5\cdot nH_2O$/rGO) cathode material that showed an impressive electrochemical performance (as opposed to the pristine Mn^{2+} inserted hydrated vanadium pentoxide nanobelts (MnVOH)), with an outstanding capacity of 361 mA h g^{-1} at 0.1 A g^{-1}. The synergistic effect of the Mn^{2+} insertion and the highly conductive rGO guarantees excellent electrochemical performance.[37] In addition, Dong and Meng's group developed a composite of Ca^{2+}-intercalated hydrated and reduced graphene oxide (CaVOH/rGO) using the hydrothermal method.[38] The rGO framework facilitates electron-ion transport pathways, and the intercalation of calcium ions significantly increases the layer spacing of VOH and thus provides stability to the CaVOH/rGO composite. As a result, the CaVOH//rGO//Zn battery delivered a capacity of 350 mA h g^{-1} at 0.1 A g^{-1}, which was much higher than that of the pristine VOH//Zn battery with a capacity of 150 mA h g^{-1} at 0.1 A g^{-1}. Inspired by these results, we compounded single-walled carbon nanotubes (SWCNTs) into MnVOH nanoflakes to generate electron paths, thus resulting in ZIBs with advanced electrochemical performance. To the best of our knowledge, the development of metal-intercalated VOH, incorporated with SWCNTs as a cathode material for ZIB applications, has rarely been reported. Therefore, it is desirable to fabricate composites of metal-intercalated VOH integrated with SWCNTs (MnVOH@SWCNTs) as cathode materials for high-rate ZIBs.

In this study, MnVOH@SWCNT nanocomposites were synthesized *via* the scalable hydrothermal method, followed by freeze-drying. Different amounts of SWCNTs were added to MnVOH (such as 2.5, 5, and 10 wt%, which were labeled as 2.5 wt% SWCNT, 5 wt% SWCNT, and 10 wt% SWCNT, respectively), and were used as active materials for AZIB applications. Compared with pristine MnVOH, the batteries based on MnVOH@SWCNT (5 wt% SWCNT) nanocomposite material showed an excellent reversible capacity of 381 mA h g^{-1} at a current density of 0.1 A g^{-1}. They exhibited outstanding rate performance and a capacity retention of 89.2% after 300 cycles, at a high current density of 5 A g^{-1}. Furthermore, CV tests at varying scan rates and electrochemical impedance spectroscopy (EIS) analysis demonstrated that after incorporating SWCNTs into MnVOH, the electron transfer process and electrode charge distribution can be accelerated during the redox reaction of V^{5+}/V^{4+} and V^{4+}/V^{3+}. Moreover, the network structure of SWCNTs

can significantly improve the electronic conductivity and diffusion kinetics of ZIBs, along with the insertion of abundant Zn^{2+} active sites. This study indicates that the electrochemical performance of ZIBs can be improved by incorporating a highly conductive material, such as SWCNTs, with a layered MnVOH material. Thus, the as-prepared AZIBs exhibited outstanding electrochemical performance and have tremendous potential in grid-scale energy storage systems. Moreover, to investigate the Zn-ion storage mechanism of the MnVOH@SWCNT nanoparticles, advanced characterization studies such as *operando* synchrotron V K-edge X-ray absorption near-edge structure (XANES) and *operando* synchrotron X-ray diffraction (XRD) measurements were performed. The *operando* XANES results indicated that the redox reactions of V ions occurred continuously and reversibly during the intercalation/deintercalation processes of Zn^{2+} ions, thus resulting in high Zn-ion storage capability and excellent cycling stability. In addition, *operando* XRD demonstrates the expansion and contraction of the interlayer spacing during the discharging and charging processes, indicating the high reversibility that leads to stable cycling capability.

Experimental methods

Synthesis of MnVOH/SWCNT nanocomposites

All chemicals were used as received without refinement. MnVOH@SWCNTs was synthesized using a one-step hydrothermal process, as shown in Fig. 1. In brief, SWCNTs (1.0–3.0 atomic% carboxylic acid; Carbon Solutions, Inc., USA) were dispersed in 11.25 ml of DI water, to which 63.38 mg of $MnSO_4 \cdot H_2O$ (99+%, extra pure, ACROS Organics) was added after using a tip sonication treatment for 30 min. The SWCNTs were added using 2.5 wt%, 5 wt%, and 10 wt% SWCNTs and the weight percentage was estimated from the weight of MnVOH. Later, 136.39 mg of V_2O_5 (99.3%, SHOWA) was dissolved into 18.75 ml of DI water with 0.75 ml of H_2O_2 (30%, Fisher Chemical). Both solutions were mixed and transferred into a 50 ml Teflon-lined stainless-steel autoclave and heated at 120 °C for 6 h. The hydrothermal reactor was allowed to naturally cool to room temperature. The precipitates were collected by washing the obtained product with DI water and ethanol several times by centrifugation at 2000 rpm for 10 min. Subsequently, the collected precipitates were transferred to a freezer operating at −80 °C for 24 h with the addition of 10 ml of DI water to achieve complete freezing. The frozen materials were lyophilized (Labconco) for 48 h to obtain a sublimate of the frozen solvent. The lyophilized product consisted of micro-, meso-, and macroporous structures, as shown in Fig. 1. The MnVOH powder was prepared following the same procedure and processing conditions without SWCNT sources.

Material characterization studies

Field emission scanning electron microscopy (FESEM, Hitachi SU8010) and scanning transmission electron microscopy (STEM, JEOL JEM-F200) with energy dispersive X-ray spectroscopy (EDX) were used to investigate the morphological characteristics of the samples. The structures of the MnVOH nanoflakes and MnVOH@SWCNT nanocomposites were characterized using X-ray diffraction (XRD, Bruker D2 Phaser). The surface area was estimated by Brunauer–Emmett–Teller (BET) analysis of the N_2 adsorption–desorption isotherms obtained at

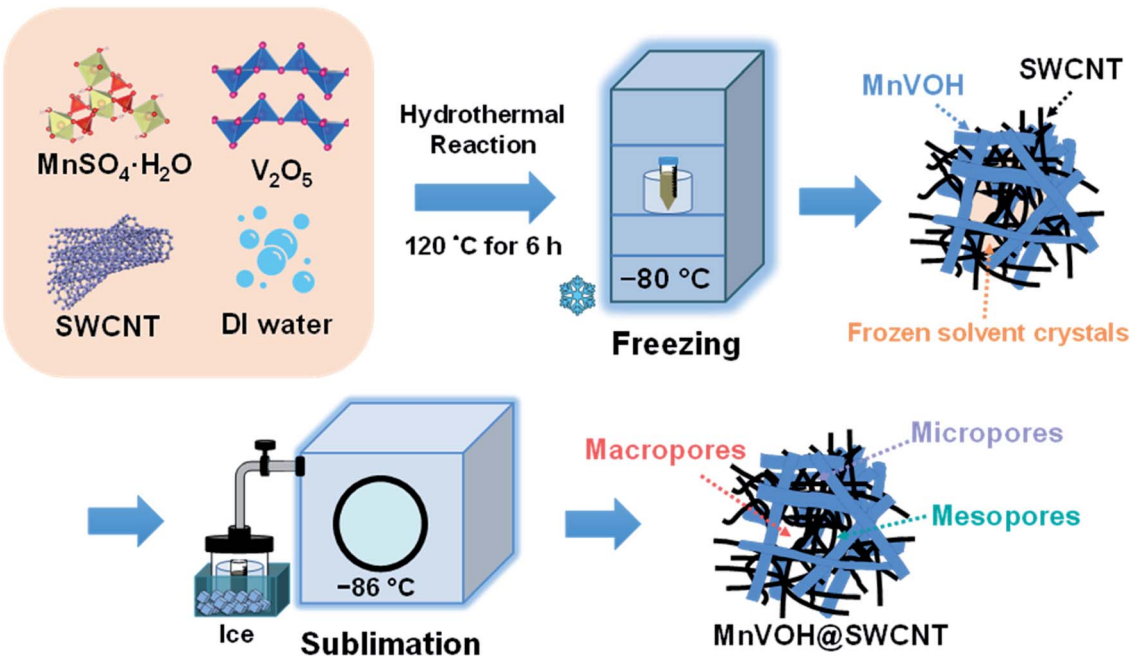

Fig. 1 Schematic illustration of the freeze-drying process utilized to achieve the different pore-sized structures for pristine MnVOH and the MnVOH@SWCNT nanocomposite.

77 K (ASAP 2020, Micrometric Corp). The Raman spectra were recorded using a confocal microscope Raman spectroscopy system (Ms 35041, UniDRON). Thermogravimetric analysis (TGA) was performed using a thermal analyzer (TG/DTA 6300, PerkinElmer) in an argon environment with a 60 ml min^{-1} flow and a temperature range of 25–550 °C at a rate of 5 °C min^{-1}. Inductively coupled plasma optical emission spectrometry (ICP-OES, Aglient-600) was used to approximate the composition of the as-synthesized materials.

Electrochemical characterization studies

The electrodes were obtained by admixing the active materials such as MnVOH/2.5 wt%SWCNT/5 wt%SWCNT/10 wt% SWCNT/SWCNT, super-P, and polyvinylidene fluoride (PVDF) in a mass ratio of 7 : 2 : 1 with *N*-methyl-2-pyrrolidone (NMP) as the solvent. The obtained slurry was then coated on carbon paper (40 μm) as a current collector and heated at 110 °C in a Buchi oven under vacuum to remove NMP from the coated slurry. To investigate the electrochemical performance of the as-prepared materials, stainless-steel CR2032 coin cells were assembled in an air environment. The cells were assembled using MnVOH, SWCNTs, and MnVOH@SWCNT composites as the cathode, a glass fiber filter (Whatman, Grade GF/A) as the separator, Zn foil (thickness ~100 μm) as the anode, and 3 M aqueous $Zn(CF_3SO_3)_2$ solution as the electrolyte. The loading mass of the active material was ~2 mg. Cyclic voltammetry (CV) tests (in a voltage range of 0.2–1.6 V), the potentiostatic intermittent titration technique (PITT), and electrochemical impedance spectroscopy (EIS) measurements (in a frequency range of 100 kHz to 100 0.01 Hz) were performed on a Biologic VMP3 potentiostat for the electrode material. Galvanostatic charge/discharge (GCD) tests were performed using a NEWARE battery-testing system. The surface chemical compositions of the powder and electrodes were confirmed using X-ray photoelectron spectroscopy (ECSA, ULVAC-PHI 5000 Versaprobe II) with monochromatized Al Kα X-rays ($h\nu = 1486.6$ eV). *Operando* synchrotron XRD and *operando* V K-edge XANES measurements were conducted at the TPS 19A and TLS 17C1 beamlines, respectively, at the National Synchrotron Radiation Research Center (NSRRC) in Taiwan. Moreover, XANES measurements were performed using a CR2032 coin cell with a hole 5 mm in diameter in fluorescent mode. The software package Athena was used for processing the V K-edge XANES data.

Results and discussion

Composition and morphology of MnVO@SWCNTs

The MnVOH@SWCNT and MnVOH materials were synthesized by a simple process comprising a facile hydrothermal method, followed by freeze-drying, as schematically presented in Fig. 1. The experimental section provides a detailed description of the approach. The nanocomposites were characterized using field emission scanning electron microscopy (FE-SEM), transmission electron microscopy (TEM), Raman spectroscopy, Brunauer–Emmett–Teller (BET) theory, and energy dispersive X-ray (EDX), inductively coupled plasma (ICP), thermogravimetric (TGA), and X-ray photoelectron spectroscopy (XPS) analyses. Fig. 2, S1 and S2† shows the FE-SEM, XRD and TEM-EDS images of the pristine MnVOH, MnVOH@SWCNT, and SWCNT materials. Fig. 2(a)–(c) shows the FE-SEM images of the MnVOH@SWCNT (2.5 wt% SWCNTs, 5 wt% SWCNTs, and 10 wt% SWCNTs) nanocomposites. MnVOH exhibited nanoflake morphology, as shown in Fig. S1(a) and S2(a).† The size of the as-received SWCNTs was approximately 1–1.5 μm, as shown in Fig. S1(b) and S2(c).† After the addition of SWCNTs, MnVOH nanoflakes were incorporated into the SWCNT network. The conjunction of SWCNTs with MnVOH can be clearly seen in all the nanocomposite materials (Fig. 2(a)–(c)). The high-resolution transmission electron microscopy (HRTEM) image of the 5 wt% SWCNT nanocomposite material (Fig. S2(b)†) also shows the presence of SWCNTs in the MnVOH nanoflakes. The SWCNTs formed a highly conductive interconnected network with the MnVOH nanoflakes. MnVOH and SWCNTs build carbon bridges that enhance the electron transfer rate in all nanocomposite materials. The elemental distributions can be seen from the EDS mappings collected by TEM, as shown in Fig. 2(g) and S1(e),† thus confirming that V, O, and Mn were well distributed in pristine MnVOH, while C, V, O, and Mn were well distributed in the 5 wt% SWCNT nanocomposite cathode material. It can be clearly seen that SWCNTs act as an electronic conducting network inside MnVOH, which suggests the incorporation of SWCNTs with MnVOH nanoflakes.

The crystal structures of MnVOH@SWCNTs (2.5 wt% SWCNTs, 5 wt% SWCNTs, and 10 wt% SWCNTs) and MnVOH were studied using XRD measurements, as presented in Fig. 2(d). All the characteristic peaks match the previously reported cation-inserted (*viz.*, Al^{3+}, Mn^{2+}, Cu^{2+}, Mg^{2+}, and K^{+}) $V_2O_5 \cdot nH_2O$ material.[7,12,21,22] Moreover, the XRD patterns of all materials showed a strong peak at $2\theta < 10°$ corresponding to the (001) lattice plane, thereby suggesting the formation of a layered crystal structure. The strongest peaks with $2\theta = 6.4°$, 6.6°, 6.6°, and 6.5° corresponding to MnVOH, and 2.5, 5, and 10 wt% SWCNTs, respectively, were related to the large interlayer spacings of 13.8 Å, 13.4 Å, 13.4 Å, and 13.6 Å, respectively. Such large interlayer spacing values enhance Zn^{2+} ion diffusion into the interlayers of these materials and contribute to enhanced capacity. The typical lattice fringes for the MnVOH@SWCNTs (5 wt% SWCNT) can be examined in the HR-TEM image shown in Fig. 2(e) and (f). An interlayer spacing of 13.3 Å can be observed, and this is related to the diffraction peak at 6.64° in the XRD pattern based on the Bragg equation with wavelength $\lambda = 1.54$ Å. In addition, the HRTEM image shown in Fig. 2(f) shows an interfering spacing of 3.4 Å, which was further confirmed by the selected area electron diffraction (SAED) pattern and is in accordance with the peaks at 25.56° in the XRD pattern. Moreover, pristine MnVOH also shows interlayer spacings of 13.8 Å and 3.4 Å, which correspond to the (001) and (110) planes (Fig. S1(c) and (d)†). However, the interlayer spacing obtained from the XRD data was significantly higher than that measured from the corresponding TEM data. This may be caused by the contraction of the interlayer spacing during the HR-TEM experiment as a result of the evaporation of

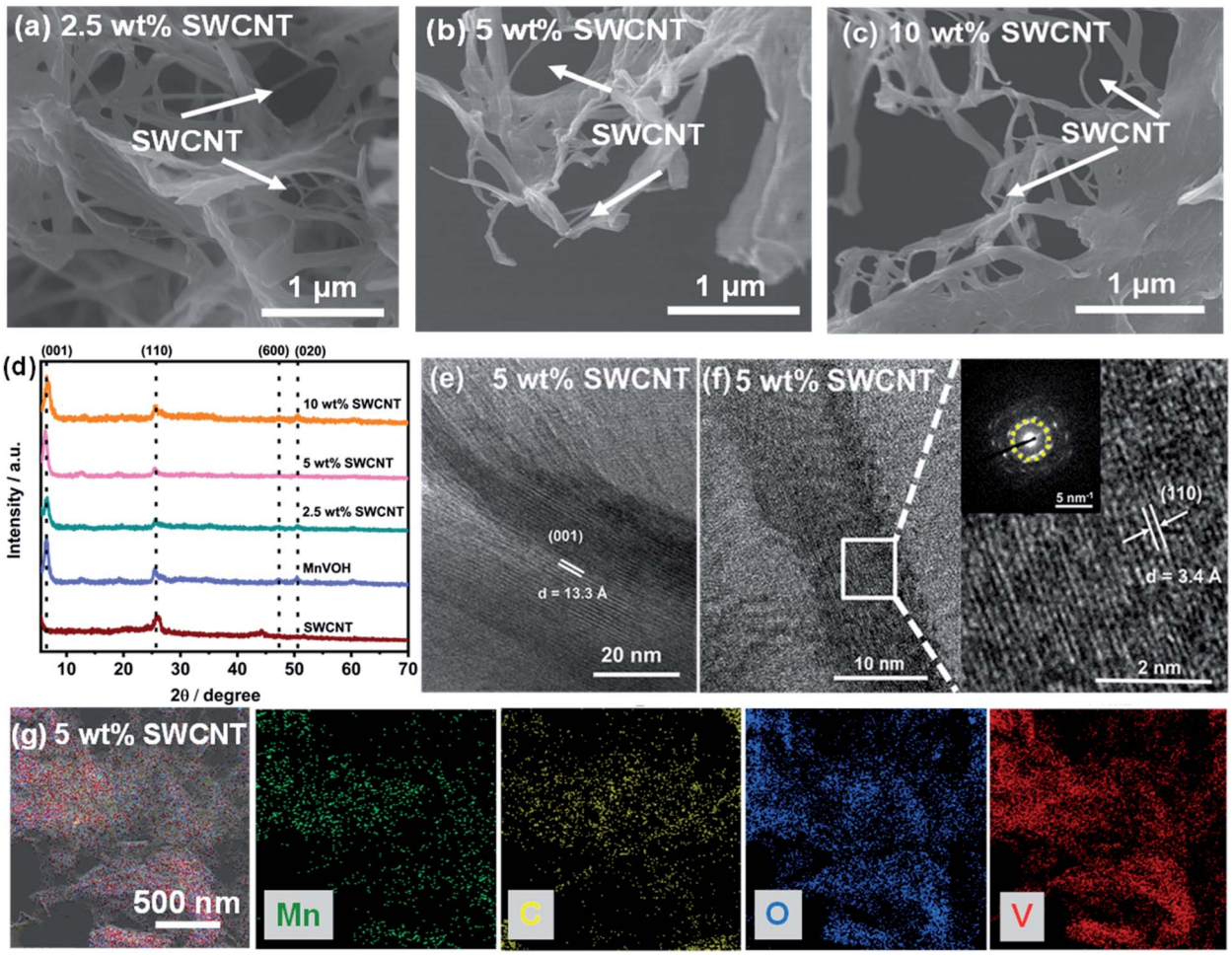

Fig. 2 FESEM images of the various electrode materials: (a) 2.5 wt% SWCNTs; (b) 5 wt% SWCNTs; and (c) 10 wt% SWCNTs. (d) XRD patterns of SWCNTs, MnVOH, 2.5 wt% SWCNTs, 5 wt% SWCNTs, and 10 wt% SWCNTs. HRTEM images of 5 wt% SWCNTs: (e) 13.3 Å interlayer spacing; (f) 3.4 Å interlayer spacing (inset is the SAED pattern). (g) TEM-EDX mapping images of 5 wt% SWCNTs.

the interlayer water molecules under the very strong electron beam in vacuum.[27]

The specific surface areas of the MnVOH@SWCNT nanocomposites and pristine MnVOH material were further determined by applying the BET theory to the N_2 adsorption/desorption isothermal curves. As shown in Fig. 3(a) and S3(a),† the surface areas of MnVOH, 2.5 wt% SWCNTs, 5 wt% SWCNTs, and 10 wt% SWCNTs were 11.9, 8.5, 8.8, and 4.1 $m^2 g^{-1}$, respectively. Based on these results, it is reasonable to conclude that the surface area of the MnVOH@SWCNT nanocomposites decreased after the addition of the SWCNTs. This was anticipated because of the coalescence effect. Moreover, the average pore size for MnVOH, 2.5 wt% SWCNTs, 5 wt% SWCNTs, and 10 wt% SWCNTs were 11.04, 13.41, 10.94, and 15.16 nm, respectively, as shown in Fig. S3(b).† Fig. S3(c)† shows the total pore size distribution for all micro-, meso-, and macro-sized materials. Also, Fig. 3(b) shows the number ratios of micropores, mesopores, and macropores for MnVOH and MnVOH@SWCNTs. The content of mesopores in MnVOH, 2.5 wt% SWCNTs, 5 wt% SWCNTs, and 10 wt% SWCNTs were calculated to be 85.6%, 64.5%, 96.1%, and 80.1 percent,

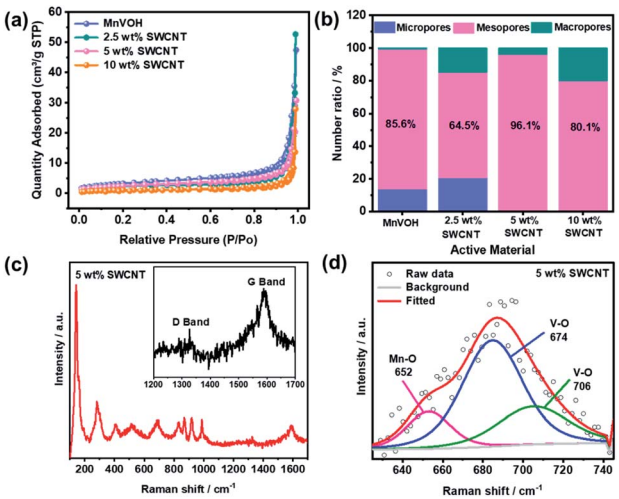

Fig. 3 BET analyses of MnVOH, 2.5 wt% SWCNTs, 5 wt% SWCNTs, and 10 wt% SWCNTs: (a) N2 adsorption–desorption isotherms; (b) BET surface area. Raman spectrum: (c) 5 wt% SWCNTs (inset is the spectrum from 1200 to 1700 cm^{-1}), and (d) partially fitted spectra to show the presence of the Mn–O bond.

respectively. It can be seen that the 5 wt% SWCNTs showed the highest surface area of 8.8 $m^2\ g^{-1}$ and the most significant number of mesopores that were more accessible for Zn^{2+} transport in MnVOH flakes (96.1%). Thus, the improvements in electrochemical performance for 5 wt% SWCNTs are expected to be greater because of the highest surface area and mesopore percentage among the nanocomposite materials. The structural characteristics of the materials were confirmed using Raman spectroscopy, TGA analysis, inductively coupled plasma optical emission spectrometry (ICP-OES), and XPS. As shown in Fig. 3(c), the Raman spectrum of MnVOH@SWCNTs (5 wt% SWCNTs) shows the presence of D and G bands, as compared to that of MnVOH), and evidently shows the presence of SWCNTs in the composite material (inset of Fig. 3(c)).[35] Compared with SWCNTs (1562 cm^{-1}) (Fig. S4(a)†), the G-peak of the 5 wt% SWCNTs (1588 cm^{-1}) shifted to a higher frequency. This implies an increase in the compression effect after the addition of SWCNTs, thus indicating the strong combination of MnVOH and SWCNTs that can facilitate faster electron transport during cycling.[38] Additionally, the peaks located at 143, 282, 700, and 988 cm^{-1} were assigned to the V–O vibrations in both MnVOH@SWCNTs and MnVOH.[12,27,38] Besides, another weak peak appears at 652 cm^{-1} in the fitting result, as shown in Fig. 3(d), which is related to a Mn–O bond and hence reveals a strong chemical interaction between Mn and O atoms.[12] Furthermore, TGA was used to analyze the content of intercalated water in MnVOH@SWCNT (5 wt% SWCNTs) nanocomposites as compared to pristine MnVOH over a temperature range of 25–550 °C under an Ar atmosphere. As shown in Fig. S4(b),† the water loss in both samples was maintained by a constant endothermal process, evidently indicated by the two drops at 150 and 380 °C. It is worth mentioning that the final temperature for water loss from the 5 wt% SWCNT nanocomposite (475 °C) was greater than that from MnVOH (380 °C), implying that water has stronger structural stability due to the incorporation of SWCNTs in MnVOH. However, the water content of the 5 wt% SWCNT material (17 wt%) was almost the same as that of MnVOH (18 wt%). It can be assumed that both samples have an equivalent amount of water based on the variation in the resultant measurements. These results indicate that both samples have similar crystal structures and chemical states, and the expected impact of crystal water on the electrochemical performance of these samples can be eliminated.[21] Furthermore, the smaller water contact angle of 5 wt% SWCNTs implies better hydrophilicity (a decrease from 21.48° to 20.54°, Fig. S5†). ICP-OES was used to approximate the compositions of the as-synthesized pristine MnVOH and MnVOH@SWCNT nanocomposites. The atomic ratios of Mn and V were found to be approximately 0.19 : 2.0, in both the MnVOH and MnVOH@SWCNT nanocomposites. Hence, the TGA and ICP-OES results indicated that the composite existed in the form of $Mn_{0.19}V_2O_5 \cdot 2.34H_2O$. Furthermore, the weight percentage of SWCNTs in the MnVOH@SWCNT nanohybrid materials was also estimated by TGA measured in air as shown in Fig. S4(c)† and is listed in Table S2.† Although the weight percentage of SWCNTs in the final products is not exactly the same as in the precursors, the trends are similar. When the weight percentage of the SWCNT precursor increases, the amount of SWCNTs in the MnVOH@SWCNT nanohybrid also increases.

XPS was used to determine the chemical states of V, C, and O in the materials, as shown in Fig. S6.† The existence of V, C, O, and Mn can be observed in the survey spectrum, as shown in Fig. S6(a).†[22,35] The V $2p_{3/2}$, C 1s, and O 1s XPS spectra of the 5 wt% SWCNT nanocomposite powder are shown in Fig. S6(b)–(d).† The oxidation states for V $2p_{3/2}$ are V^{5+} and V^{4+} with a binding energy of 517.6 eV and 516.4 eV, respectively.[21,22,39,40] These mixed valences of V can significantly enhance the interface and structural stability of as-prepared materials. The C 1s spectrum can be fitted to five peaks located at 284.4, 285.1, 285.8, 286.9, and 289.0 eV, which are attributed to the C=C, C–C, C–O, C=O, and O–C=O functional groups, respectively.[41–44] The O 1s spectrum can be divided into six peaks located at 530.1, 530.7, 531.4, 532.3, 533, and 533.9 eV and are associated with M–O–M, M–O–H, –COO–, C=O, H–O–H, and C–O respectively.[41,43,45,46] The chemical states for pristine MnVOH and SWCNTs are shown in Fig. S7.† The XPS survey spectra demonstrate the valence states of V, O, and Mn for pristine MnVOH (Fig. S7(a)†), and the valence states of O and C for the SWCNT powder (Fig. S7(d)†). Fig. S7(b)† shows the peaks at 517.5 eV and 516.2 eV belonging to V^{5+} and V^{4+}, respectively.[21,22,40,47] The O 1s spectrum shown in (Fig. S7(c)†) can be split into three peaks located at 530.8, 530.2, and 532.4 eV associated with M–O–H, M–O–M, and H–O–H, respectively, similar to the case of the 5 wt% SWCNT nanocomposite powder. In addition, in Fig. S7(e),† the C 1s spectrum shows the functional groups attributed to C=C, C–C, C–O, C=O, and O–C=O at binding energies of 285.1, 284.4, 285.8, 286.9, and 289.0 eV, respectively. Moreover, the presence of the –COOH functional group for the 5 wt% SWCNT nanocomposite can be clearly seen in Fig. S6(d)† and it is in accordance with the functional groups for as-received SWCNTs (Fig. S7(f)†) positioned at binding energies of 531.1, 532.4, and 533.8 eV, which are associated with –COO–, C=O, and C–O functional groups, respectively.[41,43,45,46]

Electrochemical properties of MnVOH@SWCNTs

A series of electrochemical tests were conducted, as shown in Fig. 4, to demonstrate the advantages of the MnVOH@SWCNT nanocomposites as a cathode material for ZIBs. Fig. 4(a) compares the CV curves of MnVOH and MnVOH@SWCNT (5 wt% SWCNT) cathodes, collected at a scan rate of 1.0 mV s^{-1} between 0.2 and 1.6 V, *vs.* Zn/Zn^{2+}. Voltage differences in redox pairs for both the electrodes are shown in Table 1. There are two pairs of anodic/cathodic peaks in the CV curves of both cathode materials, which correspond to the different intercalation/deintercalation processes of the Zn^{2+} ions. The redox reaction in the CV test illustrates that the peak pair existing at a higher voltage (1 V) corresponds to the redox pair of V^{5+}/V^{4+} [22] and the transition of the V^{4+}/V^{3+} pair is shown at a voltage of ~0.5 V.[44] In vanadium-based layered structures, multiphase vanadium redox couples generally cause multistep electrochemical intercalation/deintercalation of Zn^{2+} charge carriers.[16,43,44,46,48,49] For the assembled ZIBs, even though both electrodes show a similar shape in the CV curve, there is a much smaller voltage

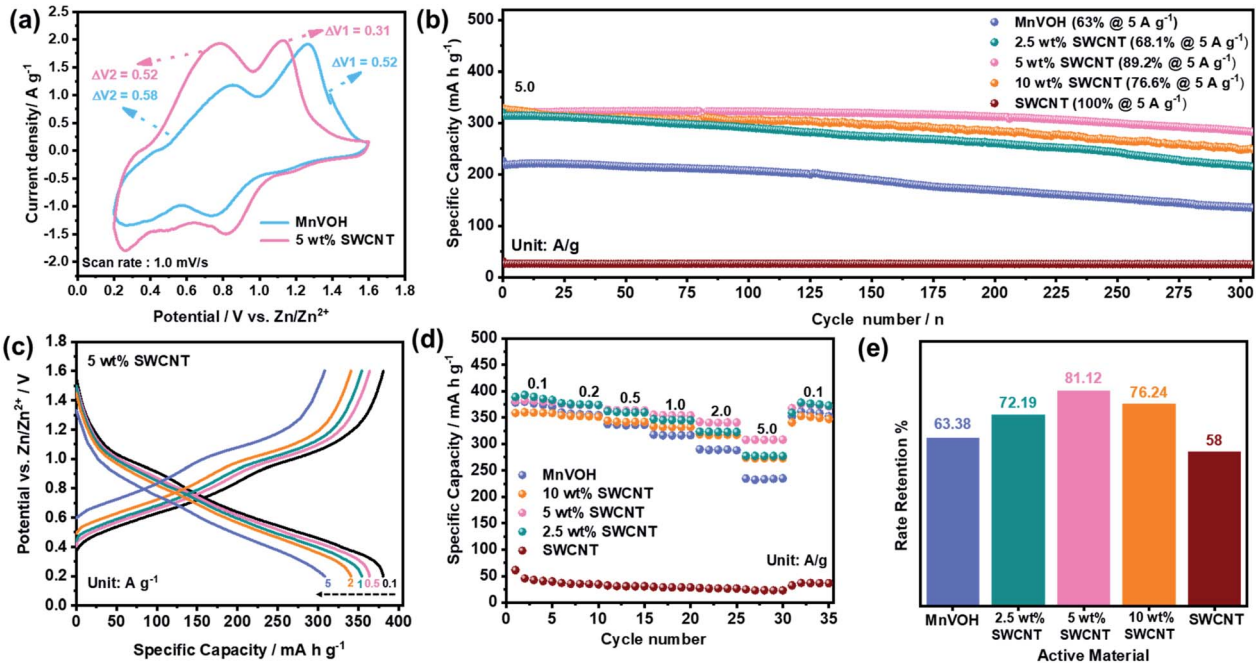

Fig. 4 Electrochemical performance: (a) comparison of the second cycle CV curves of MnVOH and 5 wt% SWCNTs at 1 mV s^{-1}. (b) Cycling performance of MnVOH, 2.5 wt% SWCNTs, 5 wt% SWCNTs, 10 wt% SWCNTs, and SWCNTs at a current density of 5 A g^{-1}. (c) Galvanostatic charge/discharge (GCD) curves for the 5 wt% SWCNT electrode at a current density of 0.1–5 A g^{-1}. (d) Comparison of rate capability (current density: 0.1–5 A g^{-1}) and (e) rate retention (current density: 5 A g^{-1} *versus* 0.1 A g^{-1}) of SWCNTs, 2.5 wt% SWCNTs, 5 wt% SWCNTs, 10 wt% SWCNTs, and MnVOH.

gap in MnVOH@SWCNTs (5 wt% SWCNTs) than in the MnVOH electrode material, which can be ascribed to faster ionic diffusion and better reaction kinetics in the electrochemical processes resulting from the addition of electrically conductive SWCNTs. Fig. S8(a)† compares the CV curves of MnVOH, SWCNTs, and MnVOH@SWCNTs (5 wt% SWCNTs) without clear redox peaks in the SWCNT electrode, implying electric double-layer capacitance (EDLC) behavior in the case of SWCNTs.

Fig. S8(b)† displays the galvanostatic charge/discharge (GCD) profiles of the MnVOH@SWCNT (5 wt% SWCNT) nanocomposite as a cathode for ZIBs at a current density of 0.1 A g^{-1} in the 1st, 2nd and 3rd cycles. The coincident GCD curves from the 1st to 3rd cycle indicate highly reversible cycling behaviors with a specific capacity of 381 mA h g^{-1} in a potential range between 0.2 and 1.6 V *versus* Zn/Zn^{2+}, corresponding to a coulombic efficiency (CE) of ~100%. This value is higher than that of pristine MnVOH (378 mA h g^{-1} at 0.1 A g^{-1}) as shown in Fig. S8(c)† and is superior to many other previously reported layered vanadium based cathode materials for ZIBs, such as $Al_{0.84}V_{12}O_{30.3}\cdot nH_2O$ (380 mA h g^{-1}),[12] $Mg_{0.34}V_2O_5\cdot nH_2O$ (352 mA h g^{-1}),[13] $CaV_6O_{16}\cdot 3H_2O$ (367 mA h g^{-1}),[15] VO_2/graphene (276 mA h g^{-1}),[17] and $V_5O_{12}\cdot 6H_2O$ (300 mA h g^{-1})[50] at a current density of ~0.1 A g^{-1}. Moreover, the performance of 5 wt% SWCNTs is quite comparable with the recently reported Zn/S (ref. 51) and Zn/Se (ref. 52) based batteries, as shown in Table S1.†

Kinetic analysis was used to investigate the electrochemical performance of the pristine MnVOH and MnVOH@SWCNT (5 wt% SWCNTs) electrode in a voltage range of 0.2–1.6 V at different scan rates of 0.1–1.8 mV s^{-1}, as shown in Fig. S9(a) and (c).† Both electrodes essentially retained well-defined oxidation/reduction peaks at various scanning rates, with a slight shift in the redox peaks as the scan rate increased, owing to the polarization effect.[22,31,37] The relationship between the current (i) and scan rates (v) is defined by the following power law equation:[25]

$$i = av^b \quad (1)$$

$$\log(i) = b\log(v) + \log(a) \quad (2)$$

where a and b are the variable parameters. When the b value approaches 0.5, the electrochemical reaction becomes diffusion-controlled. However, if b is close to 1, it is suggested that a capacitance-controlled response dominates the electrochemical process. The value of b can be obtained from the slope of the linear plot of $\log(i)$ *vs.* $\log(v)$, as shown in eqn (2). As

Table 1 Comparison of the peak position and voltage difference between pristine MnVOH and 5 wt% SWCNT nanocomposite materials

Sample ID	Peak position (V)	Voltage difference (V)
MnVOH	1.26/0.74	0.52
	0.27/0.85	0.58
MnVOH@SWCNTs	1.13/0.82	0.31
	0.26/0.78	0.52

shown in Fig. S9(b) and (d),† the calculated *b* values of peaks *a*, *b*, *c*, and *d* of MnVOH@SWCNTs (5 wt% SWCNTs) were 0.96, 0.85, 0.87, and 0.93, respectively, and those of pure MnVOH were 0.95, 0.85, 0.76, and 0.89, respectively. This suggests that both samples have significant kinetics, and the electrochemical processes were constrained by ion diffusion and capacitive-type behavior contributing to charge storage. In addition, the d/a peak, corresponding to the redox reaction of V^{5+}/V^{4+}, has a more prominent capacitive behavior than the c/b peak, and this corresponds to the redox reaction of V^{4+}/V^{3+}. Furthermore, all the peaks of the 5 wt% SWCNT electrode have higher values of *b* than those of the pure MnVOH electrode and thus, have more significant capacitance characteristics.

Furthermore, the long-term cycling stability of the MnVOH@SWCNT nanocomposites and the pristine MnVOH electrode was investigated at a high current density of 5 A g^{-1}, as shown in Fig. 4(b). The 5 wt% SWCNT nanocomposite exhibited excellent long-term cycling stability over 300 cycles with a specific capacity of 324 mA h g^{-1} and an outstanding capacity retention of 89%. This was much higher than that of pristine MnVOH (63%) and other MnVOH@SWCNT nanocomposites, that is, 2.5 wt% SWCNTs (68%) and 10 wt% SWCNTs (77%). The reason for the poor cycling stability of MnVOH might be the dissolution of V and Mn. A small amount of V (0.17 ppm) and Mn (1.94 ppm) was found in the electrolyte after cycling obtained by the ICP measurement, indicating that V and Mn may not be very stable in the MnVOH crystal structure. The CE of all the materials was ~100%, as presented in Fig. S10(a).† This was estimated for 300 cycles from the long-cycle test, thus explaining the better reversibility of the redox reactions related to the insertion/extraction process of Zn^{2+} ions. Fig. 4(c) displays the charge/discharge (GCD) curves of the 5 wt% SWCNT nanocomposite material at various current densities ranging from 0.1–5 A g^{-1}. The charge/discharge curves show excellent rate properties and a stable crystal structure, indicating the fast charge transfer kinetics of the 5 wt% SWCNT nanocomposite material. Moreover, the platforms corresponding to the V^{5+}/V^{4+} and V^{4+}/V^{3+} redox peaks were associated with the insertion/extraction of Zn^{2+} ion transport.[32,37]

In addition, the rate performance of MnVOH@SWCNT nanocomposites and pure MnVOH was investigated at different current densities ranging from 0.1–5 A g^{-1} with the same loading mass of ~2 mg for the active material, as shown in Fig. 4(d) and (e). At current densities of 0.1 A g^{-1}, the ZIBs with MnVOH as the active material, 2.5 wt% SWCNTs, and 5 wt% SWCNTs show higher capacity than those with 10 wt% SWCNTs, which can be due to the higher amount of MnVOH than in 10 wt% SWCNTs. However, at higher current densities such as 0.5, 1, 2, and 5 A g^{-1}, the 5 wt% SWCNT nanocomposite exhibited the highest capacities of 365, 355, 342, and 308 mA h g^{-1}, respectively, compared to other materials, which signifies the robustness of the 5 wt% SWCNT cathode after the addition of SWCNTs. Moreover, the cell could maintain almost the same capacity of 99% when the current density was switched back to 0.1 A g^{-1}, which signifies the robustness of the 5 wt% SWCNT cathode. Furthermore, the rate retention for the 5 wt% SWCNTs was much higher than those of the other MnVOH@SWCNT nanocomposites and pristine MnVOH cathode materials fabricated for ZIBs, as shown in Fig. 4(e). The observed rate performance (~81% retention of capacity when the current was varied from 0.1–5.0 A g^{-1}) is ascribed to the typical surface-controlled charge storage mechanism of the MnVOH@SWCNT cathode, which was discussed in the previous section.

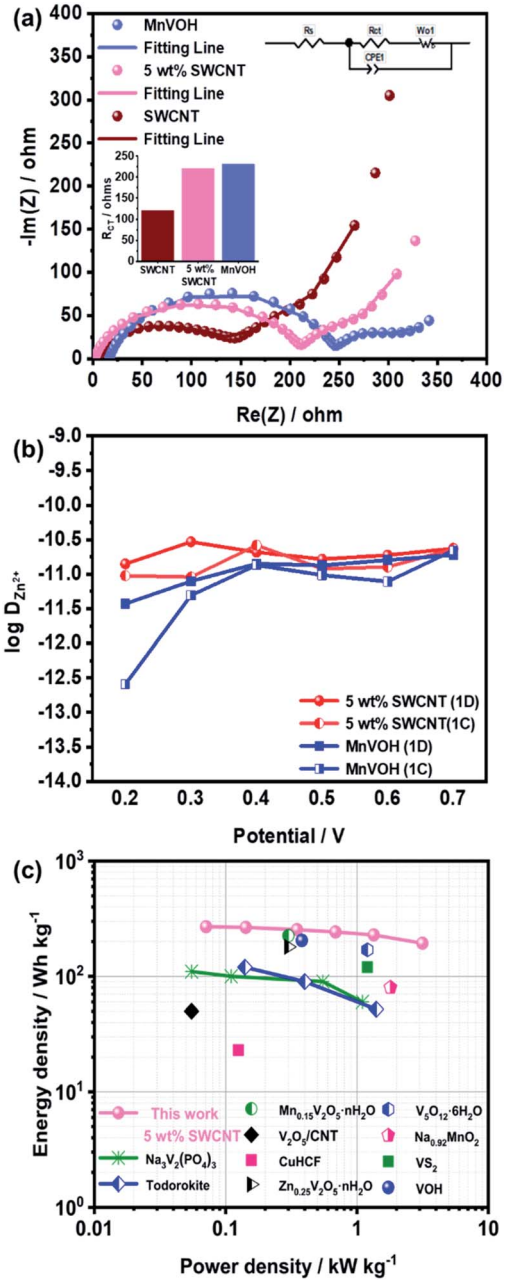

Fig. 5 (a) Nyquist plots of the SWCNT, 5 wt% SWCNT, and MnVOH electrodes. The inset shows a corresponding fitting equivalent circuit, where R_s, R_{ct}, CPE, and Wo1 represent the series resistance, interfacial charge transfer resistance, constant-phase element and Warburg diffusion process, respectively. (b) Comparison of the diffusion coefficient during the first discharge and charge process measured using the PITT method for MnVOH and 5 wt% SWCNTs. (c) Ragone plots compared with different cathode materials for aqueous zinc-ion batteries.

The superior performance of the Zn//MnVOH@SWCNT cell, especially the 5 wt% SWCNT nanocomposite, is evident from the Nyquist plots, as shown in Fig. 5(a). The charge transfer impedance (R_{CT}) of the 5 wt% SWCNT nanocomposite was 220 Ω, as depicted by the semicircle radius at a high frequency. This is much lower than that of pure MnVOH (231 Ω) and tends toward the SWCNTs (120 Ω). Hence, these results indicate that the conductivity and charge transfer kinetics can be increased by adding SWCNTs, which is further validated by the diffusion coefficient calculations (which will be discussed later).[37]

Furthermore, the diffusion coefficient was calculated using EIS measurements, during the first four cycles for MnVOH and 5 wt% SWCNT cathode materials for ZIBs, and can be defined as[53]

$$D_{Zn}^{2+} = L^2/\tau \quad (3)$$

where L is the diffusion distance based on the equation $L = V_M n_B/S$ ($V_M = 84.43$ cm^3, $n_B \approx 5.7 \times 10^{-6}$, $S = 1.33$ cm^2), and τ is the time constant for the finite diffusion process, which is given by

$$\tau = \left[\sqrt{2}\, A_w Q_t \cdot dX/dE\right]^2 \quad (4)$$

where A_w is the Warburg coefficient, which contributes to the solid-state diffusion of Zn^{2+} ions. This is based on the sloping line in the Nyquist plots in the low-frequency domain, as shown in Fig. S11(a) and (b)† for the MnVOH and 5 wt% SWCNT nanocomposites, respectively. Q_t represents the total charge involved during the insertion/extraction processes and dX/dE represents the derivative of the insertion isotherm with respect to E (potential). Moreover, in linear sweep voltammetry (LSV), $Q_t dX/dE = I_{cv}/\nu$, where I_{cv} and ν are the voltammetric current and scan rate (0.1 mV S^{-1}), respectively. Furthermore, A_w can be defined as

$$A_w = \frac{\Delta R_e}{\Delta \omega^{-1/2}} = \frac{\Delta I_m}{\Delta \omega^{-1/2}} \quad (5)$$

where R_e and I_m represent the real and imaginary parts of the impedance, respectively, and ω denotes frequency. The calculated results for D_{Zn}^{2+} are shown in Fig. S12† for the MnVOH and 5 wt% SWCNT cathodes and are in the range of 10^{-9} to 10^{-10} cm^2 s^{-1}.

In addition, the ion diffusion coefficient (D_{Zn}^{2+}) of the MnVOH and MnVOH@SWCNT (5 wt% SWCNT) electrode materials was also calculated using the potentiostatic intermittent titration technique (PITT) for discharging (1D) to 0.2 V from OCV. This was followed by charging (1C) to 1.6 V for one cycle and is based on the following equation:[53,54]

$$D_{Zn}^{2+} = \frac{d\ln(I)}{dt} \cdot \frac{4L^2}{\pi^2} \quad (6)$$

In eqn (6), I, t, and L represent the step current, step time, and diffusion distance, respectively. L is calculated in the same way as highlighted in the EIS measurement technique described in the previous section. Fig. S11(c) and (d)† show the plots of $\ln(I)$ *vs.* dt from eqn (6) for the MnVOH and 5 wt% SWCNT cathodes during the first charging process at different voltages (0.2, 0.3, 0.4, 0.5, 0.6, and 0.7 V). The slope of the plots represents the value of $d\ln(I)/dt$. The calculated D_{Zn}^{2+} of the 5 wt% SWCNTs is shown in Table S3† (first discharge), as compared to other studies in the literature. Table 2 summarizes the diffusion coefficients for the MnVOH and MnVOH@SWCNT (5 wt% SWCNT) nanocomposites obtained using the PITT method.

Table 2 Zn^{2+} diffusion coefficient of ZIB cathode materials using the PITT method

Material	Zn^{2+} diffusion coefficient (cm^2 s^{-1})/1D	Zn^{2+} diffusion coefficient (cm^2 s^{-1})/1C
5 wt% SWCNT	10^{-11}	10^{-11} to 10^{-12}
MnVOH	10^{-11} to 10^{-12}	10^{-11} to 10^{-13}

As shown in Fig. 5(b), the 5 wt% SWCNT nanocomposite material exhibits D_{Zn}^{2+} in the order of 10^{-11} to 10^{-12} cm^2 s^{-1}, which is much higher than that of MnVOH (10^{-11} to 10^{-13} cm^2 s^{-1}) and thus surpasses other reported similar cathode materials for ZIBs.† The higher value of D_{Zn}^{2+} in the 5 wt% SWCNT nanocomposite material guarantees a fast redox reaction, which endows an excellent rate performance and better cycling stability at a high current density of 5 A g^{-1}, as shown in Fig. 4(b)–(d), respectively. It was also revealed that the addition of SWCNTs played a better role in accelerating Zn-ion intercalation in aqueous zinc ion batteries. Moreover, the energy density of the ZIBs was obtained using the formula of $E = 1/m \int iV dt$, where i, dt, V, and m represent the discharge current, discharge time, voltage, and mass of active material on the cathode, respectively. Correspondingly, 5 wt% SWCNTs possess a high energy density of 269.3 W h kg^{-1} at 71 W kg^{-1}, which is based on the mass of the active material on the cathode, as shown in Fig. 5(c) in the Ragone plot. This is much larger than that of pristine MnVOH (266.5 W h kg^{-1} at 72 W kg^{-1}), as shown in Fig. S10(b),† and is much higher than various recently reported ZIB cathodes, such as $Na_3V_2(PO_4)_3$,[34] Todorokite,[55] V_2O_5/CNT,[35] $Mn_{0.15}V_2O_5 \cdot nH_2O$,[28] $Zn_{0.25}V_2O_5 \cdot nH_2O$,[56] $Na_{0.95}MnO_2$,[57] CuHCF,[57] VOH,[12] VS_2,[57] and $V_5O_{12} \cdot 6H_2O$.[7] Moreover, 5 wt% SWCNTs exhibited a high power density of 3150 W kg^{-1} at 193.6 W h kg^{-1}, with excellent potential for high-rate and large-scale ZIBs. Table 3 shows a comparison of the electrochemical kinetics of MnVOH and the 5 wt% SWCNT nanocomposite electrode, which is the best candidate for comparison, for aqueous ZIBs. The superiority of the MnVOH@SWCNT (5 wt% SWCNT) nanocomposite can be clearly observed.

Charge-storage mechanism studies

The charge storage mechanism was investigated using *in situ* and *ex situ* characterization of the MnVOH@SWCNT (5 wt% SWCNT) composite electrode. Ghosh *et al.* examined the oxidation state of V in a completely discharged/charged state in Mn-doped hydrated vanadium oxide using *ex situ* XPS measurements. They found that V 2p could be reduced from V^{5+}

Table 3 Illustration of the electrochemical performances of the pristine MnVOH and 5 wt% SWCNT nanocomposite electrodes

Material	MnVOH	MnVOH@SWCNTs (5 wt% SWCNTs)
Polarization/(voltage gap)	0.52/0.58	0.31/0.52
Specific capacity at 0.1 A g^{-1}	378 mA h g^{-1}	381 mA h g^{-1}
Rate retention (5 A g^{-1} *vs.* 0.1 A g^{-1})	63%	81%
Charge transfer resistance (Ω)	231	220
Energy density	146 W h kg^{-1}	194 W h kg^{-1}
Power density	3.1 kW kg^{-1}	3.2 kW kg^{-1}
Specific capacity at 5 A g^{-1}	277 mA h g^{-1}	324 mA h g^{-1}
Cyclic retention	63% (300 cycles)	89% (300 cycles)

to V^{4+} during cycling.[27] In contrast, Cao *et al.* reported that the oxidation state of V 2p is 4+ and 3+ in the discharge state while in the fully charged state, the oxidation state changes to 5+ and 4+, which is inconsistent with the report by Ghosh's group.[22] Besides, *ex situ* measurements are not accurate because of atmospheric sensitivity. Hence, to the best of our knowledge, *operando* measurements were performed for the first time in aqueous zinc-ion battery systems to determine the exact redox processes during insertion and extraction of Zn^{2+}.

To investigate the oxidation states during the insertion/extraction processes of Zn^{2+} more accurately, *operando* synchrotron V K-edge XANES analyses of the 5 wt% SWCNT material were carried out, as shown in Fig. 6. The V K-edge XANES spectra of the 5 wt% SWCNT cathode, during the first discharge and charge processes at 0.1 A g^{-1}, are presented in Fig. 6(a). A systematic and reversible energy shift can be clearly seen in the pre-edge peaks when V ions change from OCV (1.38 V) to a lower oxidation state of 0.2 V and back to a charged state of 1.6 V.[7] The V K-edge XANES spectra of the 5 wt% SWCNT material were compared with V_2O_3, VO_2, V_2O_5 powders, and V metal foil as shown in Fig. 6(b); the shaded area is magnified and shown in Fig. 6(c). From the figure, the XANES spectra for the initial cycle with the potentials at OCV (*ca.* 1.38 V), the first discharge at 0.2 V *versus* Zn/Zn^{2+} (1D), and the first charge at 1.6 V *versus* Zn/Zn^{2+} (1C) can be distinguished. An energy shift of the absorption curves can be clearly seen during the intercalation of Zn^{2+} into the 5 wt% SWCNT cathode material, and the absorption curve returned to the original position after the deintercalation process. The edge energy of OCV is comparable to that of V_2O_5, which implies that the valence state of V in the electrode material at OCV is close to V^{5+}. Moreover, the edge energy moves towards V_2O_3 when the electrode was discharged to 0.2 V *vs.* Zn/Zn^{2+}, thus illustrating that the average valence state of V was close to V^{3+}. Subsequently, the edge energy shifts to a higher energy for V_2O_5 in the charged state of 1.6 V *vs.* Zn/Zn^{2+}, thereby indicating that V was oxidized to a higher valence state (5+). The average valence state of V in 5 wt% SWCNTs at different potentials can be estimated using a linear combination fitting of the ATHENA software, as shown in Fig. 6(d). In addition, the chemical states of the V cations were the same in the pristine MnVOH and MnVOH@SWCNT (5 wt% SWCNT) composites, as reflected from the K-edge positions (Fig. S13†). The edge energy at the OCV overlapped with that of V_2O_5, revealing that the valence of V was 5+. However, after discharging to 0.2 V, the absorption energy shifted to a lower state, which tended towards V_2O_3, and the average valence was calculated to be 3. Conversely, after charging to 1.6 V, the absorption energy of the V K-edge shifted back to its original state of V_2O_5 with an average valence of 5, thus indicating that V was oxidized from V^{3+} to V^{5+}. This result indicates that the V ion in one MnVOH@SWCNT molecule can transfer *ca.* 4 electrons, assuming that all V^{5+} ions in MnVOH@SWCNTs are reduced to V^{3+}, and a theoretical capacity of 458 mA h g^{-1} can be estimated. This is slightly higher than the experimental value. Moreover, the morphologies of the 5 wt% SWCNT pristine electrode after discharge and charge were characterized using TEM-EDX, as shown in Fig. 6(e)–(g). The nanoflakes and the conjunction between MnVOH and the SWCNTs of the 5 wt% SWCNT nanocomposites were completely maintained. Additionally, TEM-EDX elemental mapping demonstrated the stable existence of Zn^{2+} with the other elements (V, C, Mn, and O), indicating the chemical stability of the electrode after cycling. Additionally, we also tried to detect the valence change of Mn after the charging and discharging process by *ex situ* XPS, as shown in Fig. S14.† However, the amount of Mn was pretty low, and the XPS signal was almost negligible, so it is very difficult to analyze the XPS data after cycling in discharge and charged states.

To further understand the structural changes in the MnVOH@SWCNT (5 wt% SWCNT) nanocomposite material during the discharge/charge process, *operando* synchrotron XRD measurements were performed for one cycle, as shown in Fig. 7(a). The coin cell was first discharged to 0.2 V from OCV *vs.* Zn/Zn^{2+} and later charged to 1.6 V *vs.* Zn/Zn^{2+} at a current density of 0.1 A g^{-1}, as shown in the GCD profile, obtained during the *operando* XRD measurement, in Fig. 7(b). The reflection peaks at 5.7°, 16.3°, 21.9°, 26.5°, 42.4°, 43.4°, 44.6°, and 54.6° are signals from the background, as shown in Fig. S15.† In addition, the background profiles were obtained from the active material-free electrode, which consisted of carbon black (Super P) and polyvinylidene fluoride (PVDF) as a binder coated on the current collector with 3 M $Zn(CF_3SO_3)_2$ as the electrolyte. As shown in Fig. 7(c), while the coin cell was discharging to 0.2 V, the (001) peak located at 6.6° was reversibly shifted to ~7.4°, thereby revealing the contraction of the interlayer space. Geng *et al.* observed a similar phenomenon of contraction of the interlayer spacing for the (001) peak at 6.8° that was shifted to a higher angle during the discharging

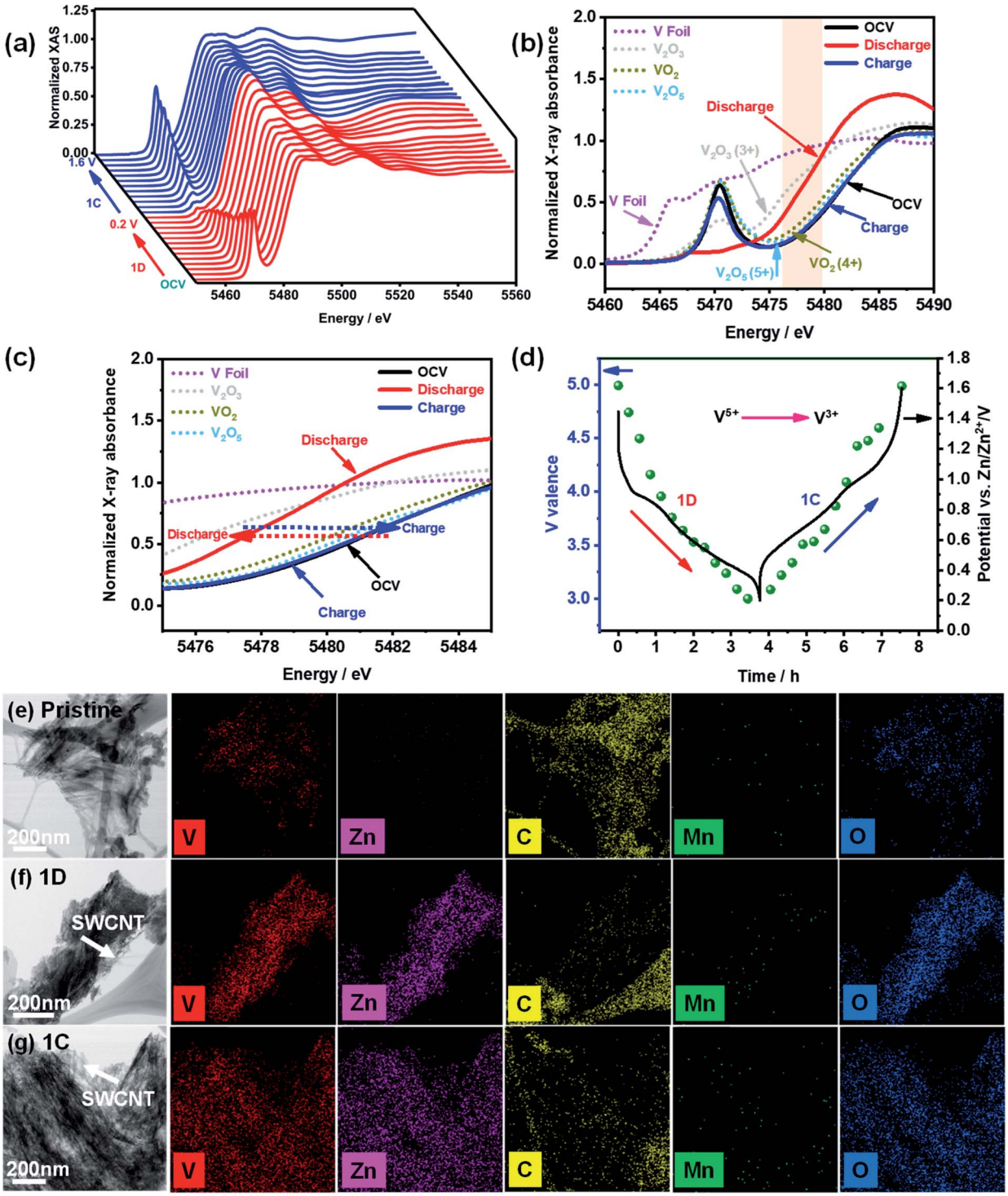

Fig. 6 (a) Normalized operando synchrotron V K-edge XANES spectra for the MnVOH@SWCNT (5 wt% SWCNT) nanocomposite. (b) Normalized operando synchrotron V K-edge XANES spectra of OCV, 1D, and 1C in comparison with V_2O_5, VO_2, and V_2O_3. (c) Magnified pattern of the shaded area in (b). (d) Average V valence of 5 wt% SWCNTs as a function of the potential. TEM-EDX elemental mapping images of 5 wt% SWCNT electrodes: (e) pristine, (f) after the first discharge (1D), and (g) after the first charge (1C).

process.[28] A possible reason for the contraction of the interlayer spacing is the decrease in interlayer repulsion and an improvement in the combination of Zn^{2+} with the structural water and oxygen from the lattice. Meanwhile, Tang *et al.*[58] also reported the same phenomenon. The (001) peak recovered to 6.3° after the charging process, indicating the high reversibility of the 5 wt% SWCNT electrode. Furthermore, five more peaks, located at 25.5°, 47.3°, 50.2°, 60.3°, and 71.2°, shifted towards a lower angle when discharged to 0.2 V, indicating the expansion of interlayer spacing. All of these peaks moved back to

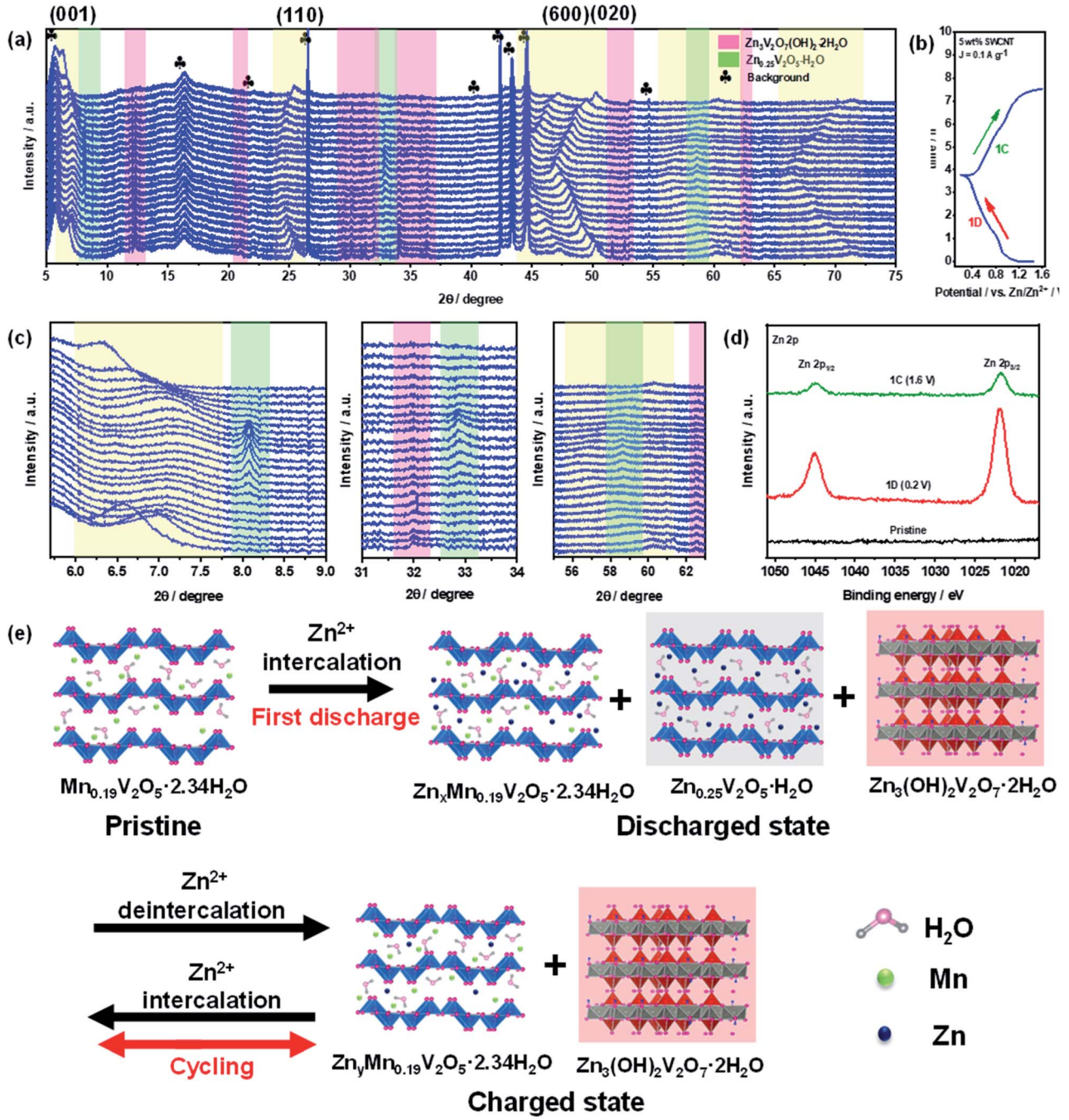

Fig. 7 Electrochemical reaction process studies. (a) and (c) Operando synchrotron radiation X-ray diffraction (XRD) patterns during the GCD process. (b) Corresponding galvanostatic charge and discharge curves at 0.1 A g^{-1}. (d) *Ex situ* XPS of Zn 2p in the pristine, discharge to 0.2 V, and charge to 1.6 V states in the first cycle. (e) Schematic illustration of the material transformation during discharge and charge in the first cycle of 5 wt% SWCNTs.

25.4°, 47.1°, 50.3°, 60.3°, and 71.5°, respectively, during the charging process at 1.6 V. Thus, this shows the high reversibility that leads to the stable cycling capability of the 5 wt% SWCNT electrode. In addition, new reversible peaks were observed at 8.2° and 32.8°, which matched well with the reversible mesophase $Zn_{0.25}V_2O_5{\cdot}H_2O$ (PDF#86-1238), as reported in a recent study.[48] Also, new peaks located at 12.3°, 20.9°, 30.1°, 34.1°, 36.4°, 51.6°, 52.6°, 62.5°, and 64.0° were indexed to $Zn_3(OH)_2V_2O_7{\cdot}2H_2O$ (PDF#-50-0570), and this was observed in previous studies.[34,37,48,58–60] Due to the enhanced binding energy between the Zn^{2+} intercalated vanadium oxide layers in the electrode material and H_2O molecules present in the electrolyte, $Zn_3(OH)_2V_2O_7{\cdot}2H_2O$ can easily grow on the electrode surface.[48,58] Additionally, Pan *et. al.* recently reported $Zn_3(OH)_2V_2O_7{\cdot}2H_2O$ as a cathode material for ZIBs with a very high performance.[61] Moreover, the formation of irreversible

$Zn_3(OH)_2V_2O_7\cdot 2H_2O$ with similar behavior was reported by Wang's group,[60] observing that the formation of irreversible phase $Zn_3(OH)_2V_2O_7\cdot 2H_2O$ can be advantageous for the migration of Zn^{2+} ions in the lattices of the cathode material with a large interlayer spacing. Hence, the cathode material is much more stable, as shown in Fig. S8(b).† In conclusion, our operando synchrotron XRD studies reveal the reversible contraction as well of expansion of the interlayer spacing of the MnVOH@SWCNT nanocomposite during the discharging/charging process which was not found in the current literature.

Furthermore, SEM-EDS was performed to determine the Zn : V ratios of the 5 wt% SWCNT electrode material after cycling (Fig. S16†). The Zn : V ratios of the discharged and charged 5 wt% SWCNT electrodes were 1.64 : 1 and 0.59 : 1, respectively. As a result, a higher portion of Zn^{2+} was entrapped into the 5 wt% SWCNT electrodes even though the amount of de-intercalated Zn^{2+} was also greater. This corresponded to its better capacity, considering that a large amount of trapped Zn^{2+} was still present in the electrode in the fully charged state. The presence of Zn^{2+} trapped in the fully charged 5 wt% SWCNT electrodes was further demonstrated by the high-resolution Zn 2p XPS spectra in the intercalated/de-intercalated state, as shown in Fig. 7(d). The trapped Zn^{2+} can serve as pillars in the crystal structure along with Mn ions. Hence, this will help in avoiding layer structure degradation and severe lattice contraction, which leads to significantly improved stability.[12] Based on the above analyses, a schematic representation of the structural transformation is provided to describe the Zn^{2+} storage mechanism during the intercalation/deintercalation process, as presented in Fig. 7(e). The above observations clearly depict the reaction mechanisms in which the original 5 wt% SWCNT ($Mn_{0.19}V_2O_5\cdot 2.34H_2O$@SWCNT) electrode was transformed into two distinct reversible phases: $Zn_xMn_{0.19}V_2O_5\cdot 2.34H_2O$ and $Zn_{0.25}V_2O_5\cdot H_2O$, with a stable $Zn_3(OH)_2V_2O_7\cdot 2H_2O$ phase during the intercalation/deintercalation of Zn^{2+}. During the discharging process, Zn^{2+} was de-intercalated to $Zn_xMn_{0.19}V_2O_5\cdot 2.34H_2O$, and during the charging process, Zn^{2+} was intercalated with $Zn_yMn_{0.19}V_2O_5\cdot 2.34H_2O$ with $y \ll x$, as anticipated from the large Zn : V ratio during discharging from the SEM-EDS results. Consequently, during the 1st discharge (1D) to 0.2 V, the Zn^{2+} in the electrolyte inserts into the layered 5 wt% SWCNT nanocomposite, thereby enlarging the lattice spacing and generating a new stable $Zn_3(OH)_2V_2O_7\cdot 2H_2O$ phase, as depicted in the *operando* XRD spectra in Fig. 7(a). On the other hand, during charging (1C) to 1.6 V, some Zn^{2+} ions leave and the lattice spacing changes back to the original size. Furthermore, the H^+ insertion plateau was not observed in the GCD curve,[62,63] and the pH value was not elevated after cycling. Besides, the formation of $Zn_x(OTf)_y(OH)_{2x-y}\cdot nH_2O$ precipitate that could lead to the formation of H^+ was not observed from operando XRD.[64] These observations indicated that the proton does not involve in the cathode reaction. Hence, the intercalation mechanism can be expressed as follows.

$$\text{Negative electrode: } Zn \rightarrow Zn^{2+} + 2e^-$$

$$\text{Positive electrode: } H_2O \rightarrow H^+ + OH^-$$

$$Zn^{2+} + Mn_{0.19}V_2O_5\cdot 2.34H_2O + H_2O + 4e^- \rightarrow Zn_xMn_{0.19}V_2O_5\cdot 2.34H_2O + Zn_{0.25}V_2O_5\cdot H_2O \text{ (reversible reaction)}$$

$$Zn^{2+} + Mn_{0.19}V_2O_5\cdot 2.34H_2O + H_2O + OH^- + 4e^- \rightarrow Zn_xMn_{0.19}V_2O_5\cdot 2.34H_2O + Zn_3(OH)_2V_2O_7\cdot 2H_2O \text{ (irreversible reaction).}$$

The formation of $Zn_{0.25}V_2O_5\cdot H_2O$ and $Zn_3(OH)_2V_2O_7\cdot 2H_2O$ was accompanied by the substitution of Zn^{2+} and Mn^{2+} ions in the electrolyte.[48] Additionally, because the $Zn_3(OH)_2V_2O_7\cdot 2H_2O$ phase remains stable owing to the presence of a hydroxyl group, it may cause capacity fading because of irreversibility.

Conclusions

In conclusion, we utilized a scalable hydrothermal synthesis method followed by freeze-drying to prepare a MnVOH@SWCNT nanocomposite as the cathode material for ZIBs. Such a configuration can provide rapid electron transfer kinetics ($D_{Zn^{2+}}$: 10^{-11} to 10^{-12} cm^2 s^{-1}) while also ensuring close interactions between MnVOH and SWCNTs during cycling. Using advanced characterization studies such as *operando* synchrotron XANES and *operando* synchrotron XRD, we studied the charge-storage mechanism for Zn^{2+} intercalation. The resultant batteries exhibited a significantly enhanced intercalation storage capacity of 381 mA h g^{-1} at a current density of 0.1 A g^{-1}, and reduced polarization with a high capacity retention of 89% over 300 cycles. Furthermore, the MnVOH@SWCNT nanocomposite exhibited an excellent rate performance of 80% during cycling. In addition, an energy density of approximately 194 W h kg^{-1}, at a high-power density of 3.2 kW kg^{-1}, was obtained which is higher than that of pristine MnVOH. Such an excellent performance can be attributed to the improvement in the conductivity of the MnVOH@SWCNT heterostructures, which may provide both continuous electron transfer pathways as well as an abundance of Zn^{2+} insertion active sites. Hence, our study provides a facile synthesis for developing a very stable and high-performance cathode material for low-cost, safe, and environmentally friendly ZIB applications.

Conflicts of interest

There are no conflicts to declare.

Acknowledgements

This work was financially supported by the Young Scholar Fellowship Program of the Ministry of Science and Technology (MOST), Taiwan under grant no. MOST 110-2636-E-007-007 (Young Scholar Fellowship Program). The authors thank the Instrumentation Center at NTHU for assisting with TEM, SEM-EDX, XRD & XPS for microstructural analyses, chemical analysis, and structural analysis. The authors also thank Dr Jyh-Fu Lee and Dr Yu-Chun Chuang at the National Synchrotron Radiation Research Center (NSRRC), Hsinchu, Taiwan for helping

with the *operando* synchrotron XAS (beamline TLS 17C) and *operando* synchrotron XRD (beamline TPS 19A) measurements.

References

1 T. M. Gür, *Energy Environ. Sci.*, 2018, **11**, 2696–2767.
2 A. Z. AL Shaqsi, K. Sopian and A. Al-Hinai, *Energy Rep.*, 2020, **6**, 288–306.
3 J. Liu, J. Wang, C. Xu, H. Jiang, C. Li, L. Zhang, J. Lin and Z. X. Shen, *Adv. Sci.*, 2018, **5**, 1700322.
4 O. Nematollahi, H. Hoghooghi, M. Rasti and A. Sedaghat, *Renewable Sustainable Energy Rev.*, 2016, **54**, 1172–1181.
5 H. Sun, G. Zhu, Y. Zhu, M. C. Lin, H. Chen, Y. Y. Li, W. H. Hung, B. Zhou, X. Wang, Y. Bai, M. Gu, C. L. Huang, H. C. Tai, X. Xu, M. Angell, J. J. Shyue and H. Dai, *Adv. Mater.*, 2020, **32**, 1–13.
6 K. Liu, Y. Liu, D. Lin, A. Pei and Y. Cui, *Sci. Adv.*, 2018, **4**, 6.
7 M. Tian, C. Liu, J. Zheng, X. Jia, E. P. Jahrman, G. T. Seidler, D. Long, M. Atif, M. Alsalhi and G. Cao, *Energy Storage Mater.*, 2020, **29**, 9–16.
8 N. Zhang, X. Chen, M. Yu, Z. Niu, F. Cheng and J. Chen, *Chem. Soc. Rev.*, 2020, **49**, 4203–4219.
9 M. H. Alfaruqi, V. Mathew, J. Gim, S. Kim, J. Song, J. P. Baboo, S. H. Choi and J. Kim, *Chem. Mater.*, 2015, **27**, 3609–3620.
10 L. Zhang, L. Chen, X. Zhou and Z. Liu, *Sci. Rep.*, 2015, **5**, 1–11.
11 F. Wan, L. Zhang, X. Wang, S. Bi, Z. Niu and J. Chen, *Adv. Funct. Mater.*, 2018, **28**, 1–8.
12 J. Zheng, C. Liu, M. Tian, X. Jia, E. P. Jahrman, G. T. Seidler, S. Zhang, Y. Liu, Y. Zhang, C. Meng and G. Cao, *Nano Energy*, 2020, **70**, 104519.
13 F. Ming, H. Liang, Y. Lei, S. Kandambeth, M. Eddaoudi and H. N. Alshareef, *ACS Energy Lett.*, 2018, **3**, 2602–2609.
14 D. Kundu, B. D. Adams, V. Duffort, S. H. Vajargah and L. F. Nazar, *Nat. Energy*, 2016, **1**, 16119.
15 X. Liu, H. Zhang, D. Geiger, J. Han, A. Varzi, U. Kaiser, A. Moretti and S. Passerini, *Chem. Commun.*, 2019, **55**, 2265–2268.
16 B. Yin, S. Zhang, K. Ke, T. Xiong, Y. Wang, B. K. D. Lim, W. S. V. Lee, Z. Wang and J. Xue, *Nanoscale*, 2019, **11**, 19723–19728.
17 X. Dai, F. Wan, L. Zhang, H. Cao and Z. Niu, *Energy Storage Mater.*, 2019, **17**, 143–150.
18 D. Chao, W. Zhou, F. Xie, C. Ye, H. Li, M. Jaroniec and S. Z. Qiao, *Sci. Adv.*, 2020, **6**, aba4098.
19 D. Chao and S. Z. Qiao, *Joule*, 2020, **4**, 1846–1851.
20 J. Liu, W. Zhou, R. Zhao, Z. Yang, W. Li, D. Chao, S. Z. Qiao and D. Zhao, *J. Am. Chem. Soc.*, 2021, **143**, 15475–15489.
21 C. Liu, M. Tian, M. Wang, J. Zheng, S. Wang, M. Yan, Z. Wang, Z. Yin, J. Yang and G. Cao, *J. Mater. Chem. A*, 2020, **8**, 7713–7723.
22 C. Liu, Z. Neale, J. Zheng, X. Jia, J. Huang, M. Yan, M. Tian, M. Wang, J. Yang and G. Cao, *Energy Environ. Sci.*, 2019, **12**, 2273–2285.
23 Y. Yang, Y. Tang, G. Fang, L. Shan, J. Guo, W. Zhang, C. Wang, L. Wang, J. Zhou and S. Liang, *Energy Environ. Sci.*, 2018, **11**, 3157–3162.
24 X. Guo, G. Fang, W. Zhang, J. Zhou, L. Shan, L. Wang, C. Wang, T. Lin, Y. Tang and S. Liang, *Adv. Energy Mater.*, 2018, **8**, 1–7.
25 M. Yan, P. He, Y. Chen, S. Wang, Q. Wei, K. Zhao, X. Xu, Q. An, Y. Shuang, Y. Shao, K. T. Mueller, L. Mai, J. Liu and J. Yang, *Adv. Mater.*, 2018, **30**, 1–6.
26 S. Liu, H. Zhu, B. Zhang, G. Li, H. Zhu, Y. Ren, H. Geng, Y. Yang, Q. Liu and C. C. Li, *Adv. Mater.*, 2020, **32**, 1–10.
27 S. Kurungot, M. Ghosh, S. Dilwale and V. Vijayakumar, *ACS Appl. Mater. Interfaces*, 2020, **12**, 48542–48552.
28 H. Geng, M. Cheng, B. Wang, Y. Yang, Y. Zhang and C. C. Li, *Adv. Funct. Mater.*, 2020, **30**, 1907684.
29 J. Hao, J. Long, B. Li, X. Li, S. Zhang, F. Yang, X. Zeng, Z. Yang, W. K. Pang and Z. Guo, *Adv. Funct. Mater.*, 2019, **29**, 1903605.
30 J. Hao, L. Yuan, B. Johannessen, Y. Zhu, C. Ye, F. Xie and S.-Z. Qiao, *Angew. Chem., Int. Ed.*, 2021, **60**, 25114–25121.
31 X. Wang, L. Wang, B. Zhang, J. Feng, J. Zhang, X. Ou, F. Hou and J. Liang, *J. Energy Chem.*, 2021, **59**, 126–133.
32 H. Chen, H. Qin, L. Chen, J. Wu and Z. Yang, *J. Alloys Compd.*, 2020, **842**, 155912.
33 G. Xu, X. Liu, S. Huang, L. Li, X. Wei, J. Cao, L. Yang and P. K. Chu, *ACS Appl. Mater. Interfaces*, 2020, **12**, 706–716.
34 H. Qin, Z. Yang, L. Chen, X. Chen and L. Wang, *J. Mater. Chem. A*, 2018, **6**, 23757–23765.
35 X. Liu, L. Ma, Y. Du, Q. Lu, A. Yang and X. Wang, *Nanomaterials*, 2021, **11**, 1–10.
36 F. Wan, S. Huang, H. Cao and Z. Niu, *ACS Nano*, 2020, **14**, 6752–6760.
37 J. Sun, Y. Liu, H. Jiang, X. Dong, T. Hu, C. Meng and Y. Zhang, *J. Colloid Interface Sci.*, 2021, **602**, 14–22.
38 T. Hu, Z. Feng, Y. Zhang, Y. Liu, J. Sun, J. Zheng, H. Jiang, P. Wang, X. Dong and C. Meng, *Inorg. Chem. Front.*, 2021, **8**, 79–89.
39 G. Silversmit, D. Depla, H. Poelman, G. B. Marin and R. De Gryse, *J. Electron Spectrosc. Relat. Phenom.*, 2004, **135**, 167–175.
40 S. Liang, Q. Shi, H. Zhu, B. Peng and W. Huang, *ACS Omega*, 2016, **1**, 1139–1148.
41 K. J. Tsai, C. S. Ni, H. Y. Chen and J. H. Huang, *J. Power Sources*, 2020, **454**, 227912.
42 P. H. Chiang, S. F. Liu, Y. H. Hung, H. Tseng, C. H. Guo and H. Y. Chen, *Energy Fuels*, 2020, **34**, 7666–7675.
43 C. S. Kam, T. L. Leung, F. Liu, A. B. Djurišić, M. H. Xie, W. K. Chan, Y. Zhou and K. Shih, *RSC Adv.*, 2018, **8**, 18355–18362.
44 H. Chen, J. Huang, S. Tian, L. Liu, T. Qin, L. Song, Y. Liu, Y. Zhang, X. Wu, S. Lei and S. Peng, *Adv. Sci.*, 2021, **8**, 2004924.
45 C. Galey and H. Park, *AIP Adv.*, 2019, **9**, 105010.
46 S. Yamamoto, H. Bluhm, K. Andersson, G. Ketteler, H. Ogasawara, M. Salmeron and A. Nilsson, *J. Phys.: Condens. Matter*, 2008, **20**, 184025.
47 G. Silversmit, D. Depla, H. Poelman, G. B. Marin and R. De Gryse, *J. Electron Spectrosc. Relat. Phenom.*, 2004, **135**, 167–175.

48 Y. Yang, Y. Tang, S. Liang, Z. Wu, G. Fang, X. Cao, C. Wang, T. Lin, A. Pan and J. Zhou, *Nano Energy*, 2019, **61**, 617–625.
49 P. He, Y. Quan, X. Xu, M. Yan, W. Yang, Q. An, L. He and L. Mai, *Small*, 2017, **13**, 1–7.
50 N. Zhang, M. Jia, Y. Dong, Y. Wang, J. Xu, Y. Liu, L. Jiao and F. Cheng, *Adv. Funct. Mater.*, 2019, **29**, 1–9.
51 Y. Zhao, D. Wang, X. Li, Q. Yang, Y. Guo, F. Mo, Q. Li, C. Peng, H. Li and C. Zhi, *Adv. Mater.*, 2020, **32**, 1–10.
52 Z. Chen, F. Mo, T. Wang, Q. Yang, Z. Huang, D. Wang, G. Liang, A. Chen, Q. Li, Y. Guo, X. Li, J. Fan and C. Zhi, *Energy Environ. Sci.*, 2021, **14**, 2441–2450.
53 C. C. Lin, C. T. Hsu, W. Liu, S. C. Huang, M. H. Lin, U. Kortz, A. S. Mougharbel, T. Y. Chen, C. W. Hu, J. F. Lee, C. C. Wang, Y. F. Liao, L. J. Li, L. Li, S. Peng, U. Stimming and H. Y. Chen, *ACS Appl. Mater. Interfaces*, 2020, **12**, 40296–40309.
54 S. C. Huang, C. C. Lin, C. T. Hsu, C. H. Guo, T. Y. Chen, Y. F. Liao and H. Y. Chen, *J. Mater. Chem. A*, 2020, **8**, 21623–21633.
55 N. Zhang, Y. Dong, M. Jia, X. Bian, Y. Wang, M. Qiu, J. Xu, Y. Liu, L. Jiao and F. Cheng, *ACS Energy Lett.*, 2018, **3**, 1366–1372.
56 J. Ding, Z. Du, L. Gu, B. Li, L. Wang, S. Wang, Y. Gong and S. Yang, *Adv. Mater.*, 2018, **30**, 2–7.
57 C. Xia, J. Guo, P. Li, X. Zhang and H. N. Alshareef, *Angew. Chem., Int. Ed.*, 2018, **57**, 3943–3948.
58 B. Tang, G. Fang, J. Zhou, L. Wang, Y. Lei, C. Wang, T. Lin, Y. Tang and S. Liang, *Nano Energy*, 2018, **51**, 579–587.
59 Q. Zong, W. Du, C. Liu, H. Yang, Q. Zhang, Z. Zhou, M. Atif, M. Alsalhi and G. Cao, *Nano-Micro Lett.*, 2021, **13**, 1–15.
60 J. Lai, H. Zhu, X. Zhu, H. Koritala and Y. Wang, *ACS Appl. Energy Mater.*, 2019, **2**, 1988–1996.
61 Z. Pan, J. Yang, J. Yang, Q. Zhang, H. Zhang, X. Li, Z. Kou, Y. Zhang, H. Chen, C. Yan and J. Wang, *ACS Nano*, 2020, **14**, 842–853.
62 Y. Dong, M. Jia, Y. Wang, J. Xu, Y. Liu, L. Jiao and N. Zhang, *ACS Appl. Energy Mater.*, 2020, **3**, 11183–11192.
63 W. Liu, X. Zhang, Y. Huang, B. Jiang, Z. Chang, C. Xu and F. Kang, *J. Energy Chem.*, 2021, **56**, 365–373.
64 L. Wang, K. W. Huang, J. Chen and J. Zheng, *Sci. Adv.*, 2019, **5**, 1–11.

